



# Photocatalytic odor abatement by platinized TiO<sub>2</sub> under optically transmitted LED–UV light



A.J. Anceno\*, R.M. Stuetz

UNSW Water Research Centre, School of Civil and Environmental Engineering, The University of New South Wales, Sydney 2052, Australia

## ARTICLE INFO

### Article history:

Received 2 September 2014

Received in revised form 16 July 2015

Accepted 20 August 2015

Available online 24 August 2015

### Keywords:

Photocatalytic deodorization

Light-emitting diode

Radiation field model

Photodegradation kinetics

Plasmonic photocatalysis

## ABSTRACT

Combined use of platinized titania and light emitting diode (LED) ultraviolet (UV) illumination was explored for photocatalytic odor abatement with carbon disulfide (CS<sub>2</sub>) as model odorant. Noble metal deposition on anatase titanium dioxide (TiO<sub>2</sub>) surface was achieved by UV assisted photoreduction of platinum (Pt). Solid-state and elemental analyses show that surface platinized (Pt/TiO<sub>2</sub>) and bare (TiO<sub>2</sub>) titania, while of comparable bulk structural properties, differ in light absorption and surface characteristics as a result of the photodeposited Pt. The effect of distance and collimation was modeled to predict the impact of position of UV source and collimation on UV radiation intensity and distribution on photocatalyst surface. Increased radiation intensity due to minimized divergence with collimated LED–UV has improved output beam intensity, resulting in enhanced photoreaction rates regardless of photocatalyst used. Fitting of batch experimental data into classical Langmuir–Hinshelwood (L–H) kinetic model yielded higher model parameter values with Pt/TiO<sub>2</sub> than TiO<sub>2</sub> as well as the calcined counterparts. Lower number of surface OH groups and better charge carrier separation in calcined and/or Pt surface treated titania were proposed as main factors underpinning enhanced reaction rates and photonic efficiencies. Data fitting into a pseudo-steady-state L–H kinetic model has returned higher optimized fit parameter values with Pt/TiO<sub>2</sub> than TiO<sub>2</sub> while showing a nonlinear power law relationship between irradiation intensity and reaction rate. Results of fluorescence excitation–emission (EEM) spectroscopy and infrared (IR) thermography corroborate the occurrence of localized surface plasmon resonance (LSPR) effects such as subdued fluorescence and localized heating. By employing plasmonic photocatalysts and innovative delivery of photoradiation, this study has presented a case of a straightforward approach to environmental odor abatement based on affordable and widely available UV–LEDs and titania support.

© 2015 Elsevier B.V. All rights reserved.

## 1. Introduction

Long-term exposure to environmental odor, whether from indoor or outdoor sources, is widely known to negatively impact human well-being with such undesirable effects including but not limited to sensory irritation, nauseous headache, fatigue, appetite loss, respiratory problems, and neurotoxic manifestations [1–6]. In most developed countries, increasing complaints and heightened public concern for better living standards has led to pertinent regulations as well as stringent limits on maximum allowed odor concentration [6]. Odor abatement can be accomplished by destructive or recuperative treatments, otherwise emissions from agro-industrial sources can be reduced by modification of processes and equipment in conjunction with treatment [7,8]. Notably

known for clean energy production and environmental depollution, advanced oxidation treatment of gas-phase pollutants based on heterogeneous photocatalysis using the low-cost and environmentally benign TiO<sub>2</sub> remains an active area of research to date [9–11]. The extensive application of this technology, however, is hindered by low photocatalytic efficiency, catalyst poisoning, and photoreactor design and operation issues.

The majority of reports on both liquid- and gas-phase photocatalysis [10,11] involve the use of low-pressure mercury tubes as photoradiation source which present safety, environmental, and sustainability concerns. Moreover, applications which require smaller scales, controlled illumination, and configuration flexibility would entail higher cost from elaborate design and engineering due to the size of fluorescent tubes [12,13]. The tremendous advancement in LED research has led to LEDs of comparable performance to fluorescent tubes with more attractive features including the availability of a range of monochromatic wavelengths, amenability to DC powering, low power requirement, tunable intensity, low

\* Corresponding author. Fax: +61 2 9313 8624.

E-mail address: [a.anceno@unsw.edu.au](mailto:a.anceno@unsw.edu.au) (A.J. Anceno).

cost for maintenance and operation, and versatile configuration and application [14]. Coupling LED light source with an optic fiber, unlike direct use of diodes themselves, allows for various possibilities in application configuration or design. Coupling LED with large numerical aperture ( $NA = \sin \theta_{\max}$ ) multi-mode optic fiber will gather most of the LED emission at the fiber input, maximizing power output at the other fiber end which serves as point accurate apparent light source. Although a considerable number of articles detail on the feasibility, kinetics and process modeling of LED based odor and volatile organics photodegradation [14], parallel studies on optic fiber coupled LED are not yet reported.

The objective of this work was to demonstrate the feasibility of use of noble metal doped titania jointly with optic fiber coupled LED whereby the alternative means of photoradiation delivery to further boost the photocatalytic deodorization capability of the LSPR sensitized (UV region) titania, while allowing flexible photoradiation source configuration. Improved photoreactivity under fiber coupled LED–UV irradiation was achieved by photoassisted surface dispersal of platinum on the surface of anatase  $\text{TiO}_2$ . This was envisaged to effect highly efficient photooxidation of model odorant  $\text{CS}_2$  by suppressing the recombination of photogenerated electrons ( $e^-$ ) and holes ( $h^+$ ) [15,16] as well as inducing LSPR effects [17–20]. Meanwhile, despite the design flexibility and maximized power output afforded by optic fiber coupled LED, issues of angular photopower gradient (i.e., of Gaussian far-field pattern) arising from the divergent emission and distance dependent attenuation of irradiance from the photoradiation source apparent remain. Collimation was hence employed as to parallelize emission and allow for spot illumination. The behavior of optically channeled LED–UV photoradiation, either uncollimated or collimated, was modeled to predict the resultant UV irradiance and distribution on photocatalyst surface. A pseudo-steady-state kinetic analysis based on earlier works [21–24] was also employed in investigating the impact of irradiance level on gas-phase  $\text{CS}_2$  photooxidation.

## 2. Methodology

### 2.1. Pt-TiO<sub>2</sub> preparation and characterization

Batch photodoping was carried out using 5 g of anatase  $\text{TiO}_2$  nanoparticles (99%, Sigma–Aldrich) and 0.052 g  $\text{H}_2\text{Cl}_6\text{Pt}$  (99.9%, ReagentPlus® Sigma–Aldrich) in 200 mL of 1% dilution of  $\text{CH}_3\text{OH}$  (sacrificial  $e^-$  donor) in Milli-Q water. The mixture was stirred (150 rpm, 2 h) under LED–UV irradiance ( $\lambda = 365$  nm,  $I_{\text{exp}} = 10 \text{ mW/cm}^2$ ,  $d = 1$  cm) as delivered from a polymer optical fiber (POF) patch cord. Grayish photodoped products were harvested by centrifugation ( $10^4$  rpm, 5 min) and dried ( $90^\circ\text{C}$ ) overnight. Portions of thus obtained Pt-TiO<sub>2</sub> as well as bare  $\text{TiO}_2$  were calcined in air at  $350^\circ\text{C}$  for 4 h. Calcined and uncalcined titania were subjected to characterization. Fourier transform infrared (FTIR) spectra were collected on a Frontier spectrometer (Perkin Elmer) equipped with diamond/ZnSe attenuated total reflectance polarizer, reflection top-plate, and pressure arm. Diffuse absorbance (DA) spectra were obtained using a Cary 100 UV–vis spectrophotometer (Agilent) equipped with an integrating sphere;  $\text{BaSO}_4$  was used as reference material. Raman spectra (RS) were recorded using an inVia Raman spectrometer (Renishaw) with an optical microscope after being diffracted by 1800 L/mm grating following 514-nm excitation from an  $\text{Ar}^+$  ion laser. X-ray diffraction (XRD) patterns were collected on X'Pert PRO multipurpose diffractometer (PANalytical) using  $\text{Cu K}\alpha 1$  ( $\lambda = 1.5406 \text{ \AA}$ ) radiation at 40 mA and 45 kV. X-ray photoelectron spectra (XPS) were obtained on an ESCALAB250Xi spectrometer (Thermo Scientific) using a monochromated  $\text{Al K}\alpha$  (1486.68 eV) operated at 50 W (13.7 kV, 4.3 mA). Pass energy was 100 eV for survey scans

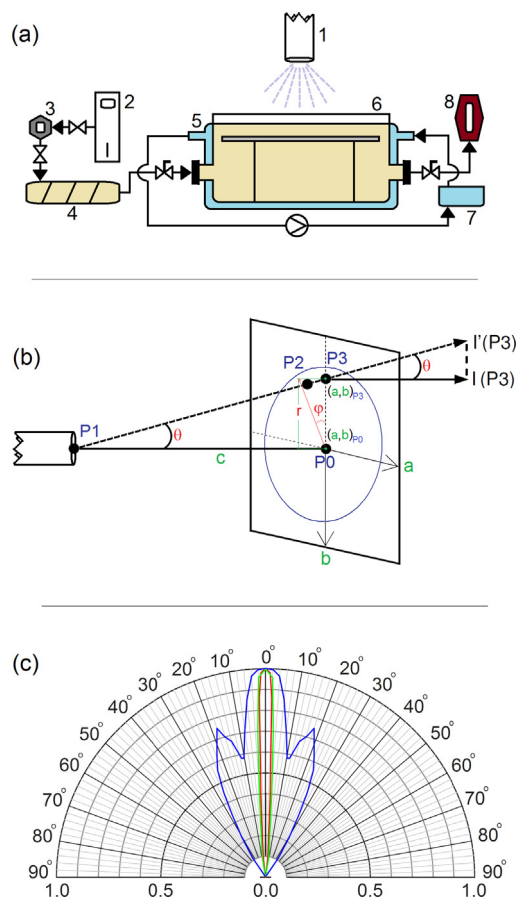


**Fig. 1.** (a) Photoreaction setup (components not to scale): optic fiber channeled UV radiation [1], dry air/nitrogen generator [2], sample loader [3], gaseous sample dilutions [4], jacketed photoreactor [5], quartz window [6], water heater [7], GC–SCD [8]; (b) schema for radiation field modeling; and (c) approximated relative directivity of non-collimated [blue], 0.5-in collimated [green], and 1-in collimated [red] LED UV radiation (365 nm). (For interpretation of the references to colour in this figure legend, the reader is referred to the web version of this article.)

and 20 eV for region scans ( $\text{Ti}2p$ ,  $\text{O}1s$ ,  $\text{C}1s$ ,  $\text{Pt}4f$ ). Binding energies were referenced to  $\text{C}1s$  (285.0 eV) of adventitious hydrocarbon. Raw fluorescence EEM spectra was collected using Cary Eclipse Fluorescence Spectrophotometer (Varian, Australia) and normalized to 20 Raman units [25]. Localized heating was monitored using a VT02 thermal imager positioned perpendicular (10 cm) to titania surface, the latter being irradiated at  $45^\circ$  angle (1 cm from optical fiber tip).

### 2.2. Photocatalysis set-up

Photoreaction cell (Fig. 1a) was made of borosilicate glass ( $r = 2.5$  cm,  $h = 4.5$  cm;  $V = 88.4$  mL). The inner surface was teflonized to prevent adsorption and outer surface jacketed for temperature control. UV radiation ( $\lambda = 365$  nm) was channeled from UV–LED source ( $P_{\text{max}} = 50$  mW, FC–LED series, Prizmatix) to the reaction cell via a POF patch cord ( $r_{\text{core}} = 750 \mu\text{m}$ ,  $NA = 0.5$ ; Mitsubishi Rayon SH6001 Super Eska™) with SMA connectors. The photocatalyst, positioned at the upper end of the cell, was accessible to UV radiation through a quartz window. Glass cover slips ( $22 \text{ mm} \times 22 \text{ mm}$ ) were used as catalyst support ( $10 \text{ mg/cm}^2$  loading). Zero air for reaction cell flushing as well as target compound dilutions was supplied by an air/nitrogen generator (Domnick Hunter) equipped with a Supelpure HC filter (Supelco). Aliquots of concentrated  $\text{CS}_2$  stock solution (99.9%, Sigma–Aldrich) or dilutions in AR grade  $\text{CH}_3\text{OH}$  (25 v%) were stored in gas-tight amber vials at  $10^\circ\text{C}$ . Gas samples at 0.5–10 ppm (8.3–166  $\mu\text{M}$ ) concentration range were prepared

by injecting appropriate volumes (0.5–10  $\mu\text{L CS}_2/\text{L}$  sample;  $4 \times$  for 25% diluted stocks) of  $\text{CS}_2$  into 3–5 Levacuated Nalophan (polyethylene terephthalate) bags using a custom-built loader. Dry zero air from the air/nitrogen generator was blown through the loader at 200–400 mL/min flow rate via a 0.25-in stainless Swagelok fitting to vaporize and dilute  $\text{CS}_2$ . Air was also bubbled through a column of sterile Milli-Q water before being supplied to the loader in experiments requiring humidity.

### 2.3. UV–LED field radiation modeling

A simplified approach to radiation field modeling (RFM) is presented for the evaluation of location-specific irradiance on the illuminated spot of photocatalyst plate in a flow-through gas-phase photoreactor. The approach surmounts the rigor of photoreactor RFM where source irradiance variability, availability, wavelength homogeneity (poly-, mono-chromaticity), and/or liquid space-phase suspended photocatalysts complicate modeling [26–28]. However, the decoupled operational condition (i.e., reactor geometry,  $[\text{CS}_2]_0$ , etc.) and photon adsorption (i.e., reaction order relative to irradiance level) feature [28,29] is retained. Here, use of POF ensures total delivery of LED photons to the catalytic surface, unlike the partial photon delivery (relative to the total emission) in an analogous system employing a tube-type source [29]. Also, the high divergence and asymmetry of emission cones when LEDs are used directly [30,31] limit possibilities in photoreaction system design. Use of a collimator minimizes irradiance gradient across the illuminated spot even at a distance. RFM assumptions were (i) insignificant optical effects (i.e., reflection, scattering, transmission) in the photoreaction chamber, (ii) nil photopower attenuation across the high-UV pass quartz window, and (iii) complete incidence of photon emission to catalyst surface. Assumptions for calculating system performance relative to irradiance levels are detailed in § 2.5.

As Fig. 1 shows, the UV source and photon receiving module (Fig. 1a) can be translated into a basic geometric schema (Fig. 1b). The angular intensity distribution (directivity) of uncollimated or collimated UV emission was determined using a digital goniometer with an attached radiometer [32–34]. Relative directivities being  $f(\theta)$  [ $0 \leq \theta < \pi/2$ ,  $0 < f(\theta) \leq 1$ ] as shown in polar coordinates (Fig. 1c) then served as the bases of field radiation modeling [26,29,31]. As detailed below, irradiance at P3 can be estimated from either Cartesian or polar coordinates.

$$c = \overline{P1P0} = \overline{P1P2} \quad (1)$$

$$\theta = \tan^{-1} \frac{\sqrt{(a_{p0} - a_{p3})^2 + (b_{p0} - b_{p3})^2}}{c} = \tan^{-1} \frac{r}{c} \quad (2)$$

$$I_{p2} = I_{p0}f(\theta) = I_{p0}f\left(\tan^{-1} \frac{r}{c}\right) \quad (3)$$

$$\begin{aligned} \frac{I'_{p3}}{(\overline{P1P2})^2} &\approx \frac{I_{p2}}{(\overline{P1P3})^2} \Rightarrow \frac{I'_{p3}}{I_{p2}} = \left(\frac{\overline{P1P2}}{\overline{P1P3}}\right)^2 = \cos^2(\theta) \\ &= \left(\frac{c}{\sqrt{c^2 + r^2}}\right)^2 \end{aligned} \quad (4)$$

$$I_{p3} = I'_{p3} \cos(\theta) = I_{p2} \cos^2(\theta). \cos(\theta) = I_{p2} \cos^3(\theta) = I_{p0}f(\theta). \cos^3(\theta) \quad (5)$$

$$I_{p3} = I_{p0}f\left(\tan^{-1} \frac{r}{c}\right) \cdot \left(\frac{c}{\sqrt{c^2 + r^2}}\right)^3 \quad (6)$$

As Eq. (6) shows, UV intensity at P3 or any location on catalyst surface can be calculated provided the intensity at the origin ( $I_{p0}$ ,  $r=0$ ) given the distance ( $c$ ), and radius ( $r$ ). Distance-specific photon power was hence determined by measuring intensity ( $I_{\text{exp}}$ ) at  $r=0$  and  $c=1$  cm using a radiometer of 0.375-cm sensor radius ( $r_{\text{exp}}$ ). With the measured intensity ( $\text{mW}/\text{cm}^2$ ) assumed as average value on the sensor [31], total incident photon power (mW) can be calculated ( $P_{\text{hv,exp}} = I_{\text{exp}}\pi r_{\text{exp}}^2$ ). Consequently, given that angle  $\phi \leq \phi_{\text{exp}}$  and  $r \leq r_{\text{exp}}$ , maximum intensity at  $c=1$  cm ( $I_{p0}^{c=1}$ ) can be obtained by solving

$$P_{\text{hv,exp}} = \int_0^{\phi_{\text{exp}}} \int_0^{r_{\text{exp}}} I_{p0}^{c=1} f\left(\tan^{-1} \frac{r}{c}\right) \cdot \left(\frac{c}{\sqrt{c^2 + r^2}}\right)^3 r d\phi dr \quad (7)$$

Thus obtained  $I_{p0}^{c=1}$  value can be used in determining irradiance at any radius with respect to the origin at a given distance as given by

$$I(r) = \frac{I_{p0}^{c=1}}{c^n} f\left(\tan^{-1} \frac{r}{c}\right) \cdot \left(\frac{c}{\sqrt{c^2 + r^2}}\right)^3 \quad (8)$$

where,  $n=2$  for uncollimated UV beam (by inverse-square law), otherwise  $n_{\text{coll}} = \pi r_{\text{sensor}}^2 / \pi r_{\text{source}}^2$  for collimated counterpart (i.e., empirical). Measurements suggested  $c^{n_{\text{coll}}}$  tended to be a good determinant of photon power attenuation for collimated UV beam.

### 2.4. Photodegradation tests

A typical batch photodegradation test started by placing the photocatalyst at an appropriate location in the photoreaction cell. Zero air was then introduced into the cell at a flow rate of 400 mL/min for 5 min. This was followed by purging 10 volumes of as-prepared gaseous dilutions of  $\text{CS}_2$  at a flow rate 50 mL/min and closing of cell inlet/outlet. To commence photoreaction, UV light at fixed distance and specific irradiance level was supplied by turning on the FC–LED machine with pre-adjusted potentiometer (i.e., predetermined power output). Since results of irradiance modeling and initial tests were consistent with regard to distance-irradiance relationship, distance of UV source apparent (fiber optic tip or collimator aperture) in later tests was adjusted such that beam spot size (2.2 cm) covers most of catalyst surface. Equivalent  $I_{\text{exp}}$  were obtained by adjusting the potentiometer.  $[\text{CS}_2]_t$  was analyzed by injecting reaction aliquots (50–100  $\mu\text{L}$ ) into a gas chromatograph (GC 7890A, Agilent) equipped with a sulfur chemiluminescence detector (SCD 355, Agilent). Sulfur species were separated using a DB–VRX column (30 m  $\times$  0.25 mm  $\times$  1.4  $\mu\text{m}$ ) with the separation program starting at 50 °C for 0.75 min and ramping at 50 °C/min–75 °C and held for 1.5 min; helium carrier gas flow rate was 6 mL/min.

### 2.5. Reaction kinetics

Assuming constant  $\text{CS}_2$  diffusivity, isothermal conditions, and that  $\text{CS}_2$  degradation follows a rate-limiting step in which surface-adsorbed  $\text{CS}_2$  reacts with transient reactive oxidants,  $\text{O}_2^{\bullet-}$  being predominant, the reaction rate is proportional to  $\text{CS}_2$  coverage of catalyst surface at steady state wherein  $[\text{O}_2^{\bullet-}]$  is held constant. Experimental data can then be fitted into Langmuir–Hinshelwood (L–H) rate expression [35]:

$$-r_0 = \frac{\partial C_0}{\partial t} = k_{\text{LH}}\theta = k_{\text{LH}} \cdot \frac{K_{\text{LH}}C_0}{1 + K_{\text{LH}}C_0} \Rightarrow \frac{1}{r_0} = \frac{1}{k_{\text{LH}}K_{\text{LH}}} \cdot \frac{1}{C_0} + \frac{1}{k_{\text{LH}}} \quad (9)$$

where,  $r_0 = \Delta C/\Delta t$  = initial photodegradation rate ( $\mu\text{M}/\text{min}$ ),  $C_0$  = initial  $\text{CS}_2$  concentration ( $\mu\text{M}$ ),  $\theta$  is surface coverage term ( $= [K_{\text{LH}}C_0]/[1 + K_{\text{LH}}C_0]$ ),  $k_{\text{LH}}$  = reaction rate constant ( $\mu\text{M}/\text{min}$ ), and  $K_{\text{LH}}$  = apparent adsorption constant ( $1/\mu\text{M}$ ).

Also, assuming an ideal match between  $\text{TiO}_2$  bandgap and incident photon energy in terms of maximal charge carrier generation as well as instantaneous carrier diffusion from bulk  $\text{TiO}_2$  through to the semiconductor–gas–phase reaction interface, quantum yield ( $\Phi$ , theoretical the reaction events per absorbed photon) is dependent only to an optimal irradiation level. Apparent photonic efficiency ( $\zeta$ , reaction events per incident photon) [36,37], in lieu of  $\Phi$ , can then be calculated using the following equation:

$$\zeta = \frac{N_r}{N_i} = \frac{(\Delta C / \Delta t) V}{\int_0^r \int_0^\varphi I(r, \varphi) r dr d\varphi / (N_a h \nu)} \quad (10)$$

where,  $\zeta$  = apparent photonic efficiency (mol/einstein),  $N_r$  = rate of  $\text{CS}_2$  converted (mol/s),  $N_i$  = rate of photons incident (einstein/s),  $C = \text{CS}_2$  concentration (mol/m<sup>3</sup>),  $V$  = photoreaction volume (m<sup>3</sup>),  $t$  = reaction time (s),  $I$  = total irradiance (W/m<sup>2</sup> = kg m<sup>2</sup>/s<sup>3</sup> m<sup>2</sup>),  $r d\varphi dr$  = UV spot area on catalyst surface (m<sup>2</sup>),  $N_a$  = Avogadro constant ( $6.022 \times 10^{23}$ /mol),  $h$  = Planck constant ( $6.63 \times 10^{-34}$  s kg m<sup>2</sup>/s<sup>2</sup>),  $\nu$  = frequency of 365 nm ( $8.22 \times 10^{14}$ /s). Preliminary tests conducted in the presence of 20–40% humidity, reported optimal for photodegradation of sulfurous odorants on titania support [38–40], has instead inhibited  $\text{CS}_2$  photodegradation. Subsequent reactions were hence carried out at room temperature in the absence of humidity.

### 3. Results and discussion

This study has employed platinumized anatase  $\text{TiO}_2$  for the simplicity of understanding observed photoreaction kinetics based on single-phase titania and metallic dopant interaction only, without having to benchmark the photocatalytic performance against P25 titania of which photocatalytic behavior could vary with preparation method and inhomogeneous crystalline composition across product batches [41]. The motivation for the use of  $\text{CS}_2$  as target odorant was its application as a major industrial precursor and fumigant as well as the limited studies in the context of plasmonic photocatalysis.  $\text{CS}_2$  is known to cause concentration dependent health effects such as acute psychophysiological symptoms (0.1–2.5 g/m<sup>3</sup>), coronary heart disease (0.03–0.12 g/m<sup>3</sup>), and hormonal disturbances ( $\sim 0.01$  g/m<sup>3</sup>), etc. [42–44]. In both occupational and environmental exposure, inhalation and/or dermal absorption constitute the major route of entry into humans.  $\text{CS}_2$  has an odor detection threshold of 200  $\mu\text{g}/\text{m}^3$  and a general exposure limit of 100  $\mu\text{g}/\text{m}^3$  in 24 h, whereas an exposure guideline of 20  $\mu\text{g}/\text{m}^3$  in 30 min is recommended for viscose emissions [43].

Presently studied  $[\text{CS}_2]_0$  range of 8.3–166  $\mu\text{M}$  (0.63–12.64 g/m<sup>3</sup>) is  $\sim 0.6$ – $1.2 \times 10^4$  times the 24-h exposure limit.  $\text{CS}_2$  is known for its two UV absorption system, namely (i) 185–280 nm at which it can photodissociate  $[\text{CS}_2 + h\nu \rightarrow \text{CS}_2^* \rightarrow \text{CS} + \text{S}]$  and further photooxidize  $[\text{CS} + \text{O}_2 \rightarrow \text{CO} + \text{SO}, \text{COS} + \text{O}]$  [45,46], and (ii) 290–380 nm at which it can photopolymerize  $[\text{CS}_2 + h\nu \rightarrow \text{CS}_2^* + \text{O}_2 \rightarrow \text{CS}_2 + \text{O}_2, \text{CS} + \text{SO}_2, \text{polymer} (\text{CS}_2)_x]$  and the polymer can further photooxidize  $[(\text{CS}_2)_x + 13\text{O}_2 \rightarrow 4\text{CO} + 2\text{COS} + 10\text{SO}_2 + [(\text{CS}_2)_{x-6}]]$  [47–49]. Atmospheric OH oxidation of  $\text{CS}_2$   $[\text{CS}_2 + \text{OH} \rightarrow \text{SH} + \text{COS}; \text{COS} + \text{OH} \rightarrow \text{SH} + \text{CO}_2]$  is also important in the formation of stratospheric sulfate layer [50,51], whilst definitive stoichiometry was under debate for some time. The role of  $\text{CH}_2\text{OH}$  adduct formation and its further oxidation  $[\text{CS}_2 + \text{OH} \leftrightarrow \text{CS}_2\text{OH}; \text{CS}_2\text{OH} + \text{O}_2 \rightarrow \text{SH}, \text{COS}, \text{HO}_2, \text{SO}_2, \text{etc.}]$  was subsequently established [52,53]. It was also reported that the adduct isomer SCS–OH is common at atmospheric condition than the theoretically more stable HO–CS<sub>2</sub> given that C-hydroxylation is thermodynamically unfavorable [54]. The relevance of these reaction pathways in titania mediated  $\text{CS}_2$  photooxidation is discussed in Section 3.4. In the mean time, we note that occurrence of photooxidation was marked by the appearance of a  $\text{SO}_2$  (64.07 g/mol) peak in GC-SCD analysis concomitant to the

disappearance of the distinct  $\text{CS}_2$  (76.14 g/mol) peak. No COS peak was detected as confirmed by running pure standards.

#### 3.1. Solid-state and elemental characterization

XRD spectra (Fig. 2a) revealed that surface platinization (0.5 wt%) and calcination (350 °C, 4 h) did not distort the crystalline structure nor shifted the crystalline phase of the commercially obtained titania which consists entirely of anatase phase (JCPDS No. 21-1272). The average crystallite size as estimated from the (1 0 1) peak using the Scherrer equation was 40–45 nm which falls within the titania nanoparticle size range (1–150 nm) indicated by the manufacturer. The presence of Raman-active fundamental modes (Fig. 2b) with the symmetries of lower  $E_g$  (145 cm<sup>−1</sup>),  $E_g$  (198 cm<sup>−1</sup>),  $B_{1g}$  (399 cm<sup>−1</sup>),  $B_{1g} + A_{1g}$  (516 cm<sup>−1</sup>), and overtone  $E_g$  (640 cm<sup>−1</sup>) indicate and confirm the crystalline framework of the titania in question. Lower peak intensities in platinized counterparts is attributed to surface adsorbed Pt which acts as electron trap that suppress  $e$ – $h$  recombination (de-excitation), a common phenomenon that occurs in the contact region between noble metal nanoparticulates and titania [55,56]. FTIR spectra (Fig. 2c) reveal similar surface patterns except the marked reduction of signals from O–H and H–O–H vibrations (3420, 1630 cm<sup>−1</sup>; [57,58]) from original titania to dried or calcined counterparts, suggesting decreasing hydroxyl groups with heat and surface platinum treatment. UV–vis diffuse reflectance spectra (Fig. 2d) show marked increase of absorption (10–35% enhancement) toward the visible and infrared region for platinized and calcined titania. The absorption edge ( $\lambda < 390$  nm) and bandgap ( $\sim 3.2$  eV) as estimated from the K–M/E plot appear typically that of anatase for all samples, whereas absorption in visible–red region resulting from heat treatment (i.e., oxygen vacancies [59]) and Pt deposition (i.e., electron trapping [59]) is accentuated. Providing an overview of the surface state of titania samples, the XPS survey spectra (Fig. 2e) prominently show the Ti2p (458–459 eV), O1s (527–532 eV), and C1s (285 eV) peaks of comparable intensities as well as the corresponding Ti<sub>LMM</sub>, O<sub>KLL</sub>, and C<sub>KLL</sub> Auger peaks. The C1s (resolved as C–H/C–C, 285 eV; C–O, 287 eV; and O–C=O, 289 eV peaks [60], not shown) and C<sub>KLL</sub> peaks likely resulted from surface contamination due to air exposure [61] which appear diminished in Pt loaded samples. The broader Ti2p doublet peaks at 455–462 eV in platinized titania accounts for the presence of Ti<sup>3+</sup> state, resulting from Pt deposition, in addition to the Ti<sup>4+</sup> state of Ti in bare counterpart with narrow Ti2p peaks at 455–461 eV (not shown). The O1s peak (resolved as O<sup>2−</sup>,  $\sim 530$  eV; OH,  $\sim 532$  eV; and H<sub>2</sub>O,  $\sim 533$  eV peaks [60]) is also broader in platinized (530–533 eV) than bare (530–532 eV) titania due to Pt treatment in aqueous condition (not shown). The Pt-specific XPS spectra (Fig. 2f) confirm the occurrence of metallic Pt ( $\sim 71$  eV) and PtO<sub>2</sub> ( $\sim 74$  eV) on the surface of platinized titania. The presence of Pt(OH)<sub>2</sub> ( $\sim 73$  eV) and PtCl<sub>6</sub><sup>2−</sup> ( $\sim 77$  eV) may also be likely [62] when chloroplatinic acid is used as Pt donor.

#### 3.2. Radiation field on photocatalytic surface

Regardless of optical fiber or collimating lens type, empirical determination of angular light intensity from an apparent light source by radiometry and use of thus obtained directivity data (see Fig. 1c) in radiation field modeling greatly simplifies estimation of irradiance on catalyst surface as a function of source position. Here we have shown a good agreement between modeled and measured irradiance profiles of uncollimated or collimated output UV beam. As shown in Figs. 3a and b, the modeled distribution and measured attenuation of irradiance in the case of uncollimated beam appears to follow the general inverse-square law with maximum irradiance value of  $\sim 75$  mW/cm<sup>2</sup> (i.e., at  $r = 0$  cm,  $d = 1$  cm). Mean-



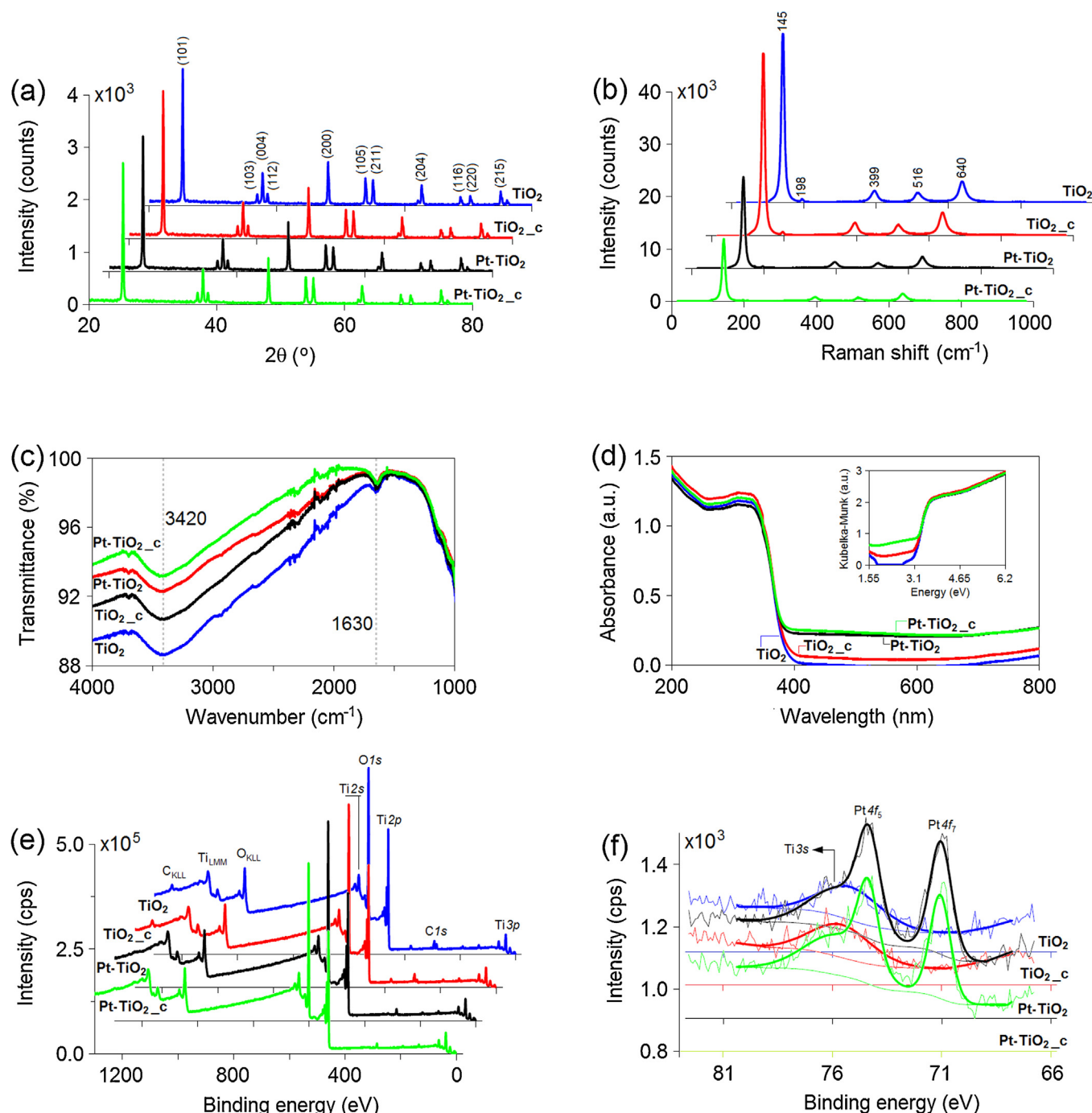


**Fig. 2.** (a) X-ray diffraction, (b) Raman, (c) Fourier transform infrared, (d) UV-vis ( $[f(R), E]^{1/2}$  transformation vs. band-gap energies inset), and (e) survey and (f) Pt-specific X-ray photoelectron spectroscopic analysis of anatase TiO<sub>2</sub> based photocatalysts. N.B.: Untreated (TiO<sub>2</sub>, blue line), calcined (TiO<sub>2</sub>-c, red line), 0.5 wt% Pt-photodoped (Pt/TiO<sub>2</sub>, black line), and calcined 0.5 wt% Pt-photodoped (Pt/TiO<sub>2</sub>-c, green line). (For interpretation of the references to colour in this figure legend, the reader is referred to the web version of this article.).

while, position-wise differences in beam divergence angles can be estimated from spot size ( $r$ -value) and distance, as also true for collimated output beam. The trend in modeled and measured far-field angular distribution of radiation intensity (Fig. 3b) appear comparable to the directivity pattern on a Cartesian plane at test distance of 10 cm, whereas the range of angle-dependent irradiance values fall within an order of magnitude. The impact of collimation was dependent on clear aperture size of the collimator used. Modeling results (Figs. 3d and g) suggested an intensified irradiance with the use of 0.5-in (11-mm aperture) collimator or weakened irradiance

with 1-in (23-mm aperture) collimator presumably due to factors dictated by geometrical optics. Nevertheless, the output beams in both cases were minimally divergent as seen from the distance-wise (0–20 cm) comparable irradiance values within an order of magnitude (Figs. 3e and h), as well as the angle-wise (3–6°) abrupt fall off of irradiance by three to four orders of magnitude (Figs. 3f and i). It appears that the tenfold reduction of output beam divergence from 60° (uncollimated) to ~6° (collimated) has enhanced irradiance value (i.e., at  $r \approx 0$  cm) by almost two-folds for the 0.5-in collimated beam.

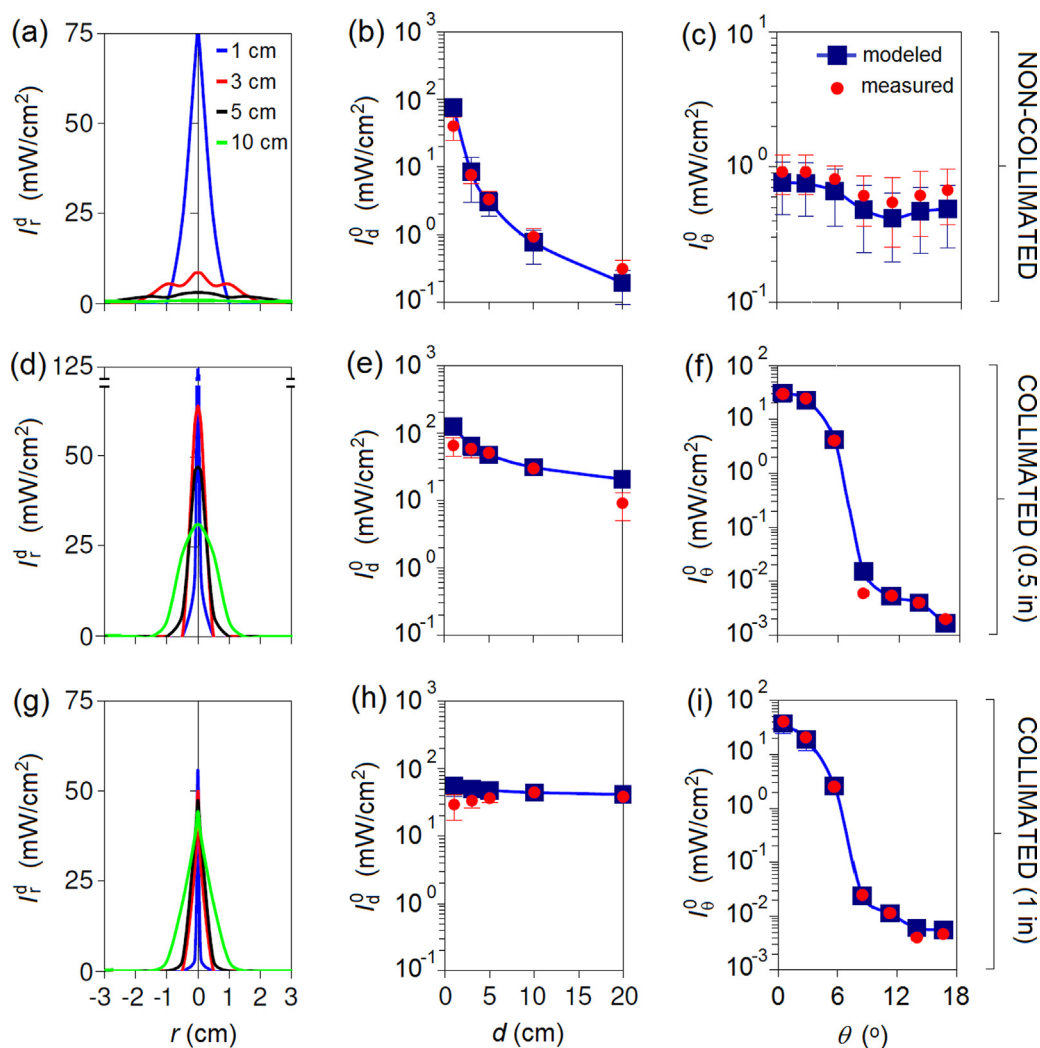


**Fig. 3.** (a, d, g) Modeled radiation intensity and distribution ( $I_r^d$ ) across the illuminated spot of catalyst surface (radius,  $r$ ) with respect to the position of UV source apparent; (b, e, h) model predicted and measured radiation intensity ( $I_d^0$ ) on catalyst surface relative to the distance ( $d$ ) of UV source apparent; and (c, f, i) model predicted and measured angle-dependent radiation intensity ( $I_\theta^0$ ) on catalyst surface from UV source apparent at  $d = 10$  cm. N.B.: Upper, middle, and lower panels are clustered according to collimation regime. (For interpretation of the references to colour in this figure legend, the reader is referred to the web version of this article.).

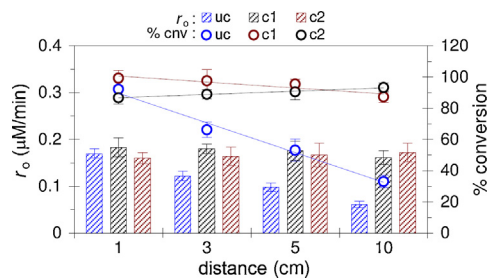


**Fig. 4.** Distance-wise  $\text{CS}_2$  conversion rates ( $r_0$ ) and efficiencies (% conversion) on bare anatase  $\text{TiO}_2$  for UV source apparent without collimation (uc), with 0.5-in collimator (c1), and with 1-in collimator (c2).  $[\text{CS}_2]_0 = 8.3 \mu\text{M}$ , reaction time = 45 min, and  $P_d = 0 \text{ cm} \approx 50 \text{ mW}$ . (For interpretation of the references to colour in this figure legend, the reader is referred to the web version of this article.).

### 3.3. Impact of collimation

Batch  $\text{CS}_2$  photooxidation experiments with bare anatase titania was carried out to verify the results of radiation field modeling (Fig. 4). Highest apparent  $\text{CS}_2$  conversion rates and efficiencies were obtained with the least distance (i.e., highest  $I_{d0}$ -value) for uncollimated (also see Fig. 3b) and 0.5-in collimated (also see

Fig. 3e) output beams. In both cases, performance was proportional to attenuated irradiance and is more pronounced with an uncollimated output of which intensity was inversely proportional to the square of distance. As for the 1-in collimated output (also see Fig. 3h), the slight performance improvement may be due to optical effects that led to a condensed output. One effect could be that of spherical aberration in which marginal rays emanating from lens periphery increasingly converge while paraxial rays maybe collimated, apparently focusing the output beam with distance. Another could be that of chromatic aberration in which the focal length of a lens increases due to a shift in refractive index (RI) of lens material as dependent on wavelength (i.e., higher RI in UV than visible region), also causing light rays to converge with distance. Despite the irradiance compensation effect of focusing, light collection on a large-aperture collimator was submaximal compared to the smaller collimator. The observed trends in batch photocatalytic performance suggest that by adjusting the distance of uncollimated POF tip, a wider catalyst surface area can be illuminated at lower irradiance, although LED photopower can be modulated at a cost for electronics and extra electricity. As for POF-coupled LEDs of fixed output photopower, use of suitable collimators would enhance irradiance on a limited catalyst surface area.

**Table 1**CS<sub>2</sub> photodegradation rates and parameter values from L–H model fitting across TiO<sub>2</sub> based photocatalysts.<sup>a</sup>

	TiO <sub>2</sub>	TiO <sub>2</sub> -c	Pt/TiO <sub>2</sub>	Pt/TiO <sub>2</sub> -c
$r_{0,s.a.}$ (M/h.m <sup>2</sup> ) <sup>b,c</sup>	0.028–0.117	0.033–0.140	0.039–0.179	0.048–0.229
$r_{0,r.v.}$ (M/h.m <sup>3</sup> ) <sup>b,d</sup>	0.121–0.502	0.143–0.602	0.170–0.772	0.204–0.988
slope <sup>e</sup>	1.778	1.539	1.289	1.095
y-intercept <sup>e</sup>	9.89	8.45	7.05	5.89
$k_{LH}$ (μM/min) <sup>e</sup>	0.101	0.118	0.142	0.170
$K_{LH}$ (1/μM) <sup>e</sup>	5.56	5.48	5.47	5.38
$1/K_{LH}$ (μM) <sup>e</sup>	0.180	0.182	0.183	0.186

<sup>a</sup> Uncollimated UV ( $d_{exp} = 2$  cm),  $I_{exp} = 10$  mW/cm<sup>2</sup>, and  $t = 25$  min.<sup>b</sup> Values correspond to increasing initial CS<sub>2</sub> concentration,  $[CS_2]_0 = 8.3$ –165.5 μM.<sup>c</sup> Catalyst surface area (s.a.) normalized initial reaction rates ( $r_0$ ).<sup>d</sup> Reaction volume (r.v.) normalized initial reaction rates ( $r_0$ ).<sup>e</sup> Obtained from  $1/r_0 - 1/C_0$  plots (see Eq. (9)).**Table 2**CS<sub>2</sub> photodegradation L–H parameter values with untreated and 0.5 wt% photodoped TiO<sub>2</sub> at different UV intensities.<sup>a,b</sup>

	TiO <sub>2</sub>		Pt/TiO <sub>2</sub>	
$I_{exp}$ (mW/cm <sup>2</sup> )	$k_{LH}$ (μM/min)	$K_{ads}^{app}$ (1/μM)	$k_{LH}$ (μM/min)	$K_{ads}^{app}$ (1/μM)
1	0.058 ± 0.008	5.83 ± 0.09	0.081 ± 0.011	5.71 ± 0.12
5	0.075 ± 0.013	5.67 ± 0.14	0.105 ± 0.016	5.57 ± 0.08
10	0.101 ± 0.024	5.56 ± 0.19	0.142 ± 0.017	5.47 ± 0.25
15	0.118 ± 0.019	5.47 ± 0.16	0.166 ± 0.022	5.39 ± 0.30

<sup>a</sup>  $[CS_2]_0 = 8.3$ –165.5 μM, uncollimated UV ( $d_{exp} = 2$  cm), and  $t = 25$  min.<sup>b</sup>  $k_{LH}$  and  $K_{ads}^{app}$  values obtained from  $1/r_0 - 1/C_0$  plots (see Eq. (9)).

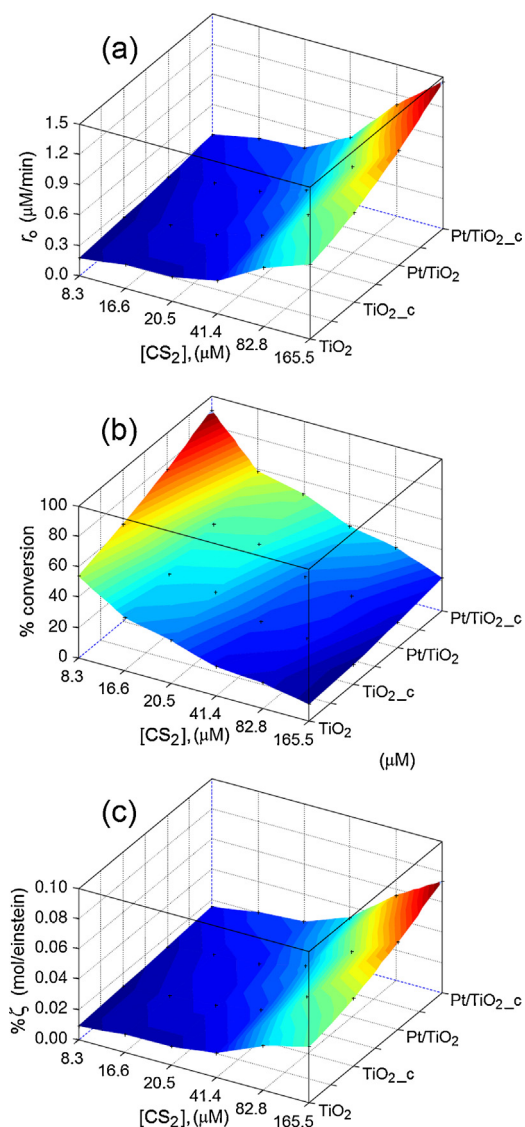
### 3.4. L–H kinetic: the photocatalyst factor

Fig. 5 shows the increase of initial reaction rates (Fig. 5a) from the use of TiO<sub>2</sub>–Pt/TiO<sub>2</sub> and calcined counterparts due to enhanced photon utilization (Fig. 5c), resulting from surface platinization and calcining. Complete conversion was also observed at sufficiently low  $[CS_2]_0$  at given experimental condition (Fig. 5b). As shown in Table 1, surface Pt treatment (0.5 wt%) of anatase TiO<sub>2</sub> has enhanced the  $k_{LH}$  by ~50% above that of bare counterpart. In both cases of TiO<sub>2</sub> and Pt/TiO<sub>2</sub>, calcination (350 °C, 2 h) has enhanced the  $k_{LH}$  by ~20%. Decreased  $K_{LH}$  with calcining and platinization indicates reduced affinity for CS<sub>2</sub> on titania surface with these treatments. An  $I_{exp}$  value of 10 mW/cm<sup>2</sup> was purposefully employed to assay the reaction kinetics at a condition where de-excitation predominates (reaction is first-order  $I_{exp}$  up to ~1 mW/cm<sup>2</sup> [24]) such that obtained  $k_{LH}$  values would be relative metric of catalyst's intrinsic capacity to circumvent de-excitation and  $K_{LH}$  descriptor of physicochemical behavior of catalyst surface. In an attempt to understand the basis of enhanced photocatalytic activity and underlying reaction mechanisms, it is critical to relate catalyst surface properties to observed reaction rates and products. Here we recall, as revealed by FTIR spectroscopy (Fig. 1c), that a progressive decrease of OH groups on titania surface would have been due primarily to calcination and secondarily to displacement by surface deposited Pt. Previous studies have shown the crucial role of OH group distribution on titania surface which defines the catalyst surface bonding environment [63,64]. Lowest number of basic terminal OH groups (i.e., terminal TiOH), as distinct from acidic bridging OH groups (i.e., bridging TiOH), was shown to coincide with highest acetaldehyde oxidation over TiO<sub>2</sub> [63]. The observation was consistent with findings of higher photocatalytic activity when acidic OH groups predominate on TiO<sub>2</sub> surface [65–67]. Interestingly, XPS analysis of present titania samples revealed that while O1s signals from physisorbed or chemisorbed O<sup>2-</sup> and H<sub>2</sub>O were consistent with oxidic calcination or aqueous preparative treatments, the O1s signals from OH has decreased in the order of TiO<sub>2</sub> (10.2 kCPS eV) > TiO<sub>2</sub>-c (9.4 kCPS eV) > Pt/TiO<sub>2</sub> (9.1 kCPS eV) > Pt/TiO<sub>2</sub>-c (8.8 kCPS eV). With irradiation at 365 nm

in zero humidity atmosphere and sufficient oxygen, it is plausible that CS<sub>2</sub> photopolymerization to oxidation-labile (CS<sub>2</sub>)<sub>x</sub> and contact with photogenerated O<sub>2</sub><sup>•-</sup> will have produced SO<sub>2</sub> and COS which was not detected whereas both compounds were shown to co-elute in SCD chromatography [68]. Assuming the predominance of acidic bridging OH groups which need to be verified, H-bonded sulfide and Ti-bonded or even Pt-bonded sulfoxide formation with subsequent oxidation by O<sub>2</sub><sup>•-</sup> to SO<sub>2</sub> and COS are a possibility. Better yet, these reaction pathways can occur simultaneously and on top of that would be the increased charge carrier lifetimes with the photogenerated electrons captured by surface deposited Pt. Crucial factors defining photocatalytic activity would hence be the distribution of desired OH groups and optimal levels of surface Pt. Here it was demonstrated that calcination and its inferred impact on titania surface distribution of OH groups effected better photocatalytic rates than surface Pt treatment alone.

### 3.5. Amended L–H kinetics: the irradiance factor

In the classic L–H kinetics, it is assumed that catalysis commences with a fast-step equilibrated adsorption of reactant and followed by a slow irreversible catalytic reaction; the latter step being known for its irradiance dependence (i.e.,  $k_{LH} = \alpha \cdot I^\beta$ ) [22]. Typically, a value of 1 and 0.5 for  $\beta$  corresponds to the dominance of reaction and de-excitation, respectively [23]. However, it was pointed out that photogenerated holes and oxygen radicals are of short lifetimes and that the opposite of the fast-desorption assumption in classic kinetics is the likely case [21]. To avoid this equilibrium assumption and allow for the evaluation of fundamental rate constants (i.e.,  $k_1$ ,  $k_{-1}$ ,  $K_{ads}$ ), given that the impact of irradiance on absorption-desorption equilibria is empirically well-supported [22–24], an amended L–H kinetic model based on pseudo-steady-state hypothesis [21] was employed. Accordingly, the dependence of overall reaction rate to irradiance was determined by fitting experimental data into an amended L–H rate



**Fig. 5.** Trends in (a)  $\text{CS}_2$  conversion rates, (b) conversion efficiencies, and (c) photonic efficiencies (see Eq. (10)) across anatase  $\text{TiO}_2$  based photocatalysts (see Fig. 1 for catalyst name abbreviation and definition).  $[\text{CS}_2]_0 = 8.3\text{--}165.5\ \mu\text{M}$ , uncollimated UV( $d_{\text{exp}} = 2\text{ cm}$ ),  $I_{\text{exp}} = 10\text{ mW/cm}^2$ ,  $t = 25\text{ min}$ . (For interpretation of the references to colour in this figure legend, the reader is referred to the web version of this article.).

expression [21,24]:

$$-r_0 = k_{\text{LH}}\theta = k_{\text{LH}} \cdot \frac{k_1 C_0}{k_1 C_0 + k_{-1} + \alpha I^\beta} = \frac{\alpha I^\beta C_0}{C_0 + \left(\frac{k_{-1} + \alpha I^\beta}{k_1}\right)} = \frac{k_{\text{LH}} C_0}{C_0 + K_{\text{ads}}^{\text{app}}} \quad (11)$$

where,  $k_{-1}/k_1 = 1/K_{\text{ads}}$  ( $=K_{\text{diss}}$ ),  $k_1$ =absorption constant,  $k_{-1}$ =desorption constant, and  $K_{\text{ads}}$ =dark Langmuir adsorption constant. Here,  $k_{\text{LH}} (= \alpha \times I^\beta)$  and  $K_{\text{diss}}^{\text{app}} (= (k_{-1} + \alpha I^\beta)/k_1)$  appear to be both dependent on level of irradiance. A plot of  $K_{\text{diss}}^{\text{app}} (= 1/K_{\text{ads}}^{\text{app}})$  versus  $k_{\text{LH}}$  will yield a slope ( $1/k_1$ ) and an intercept ( $k_{-1}/k_1$ ) as per Eq. (12). The  $I$ -independent reaction rate ( $\alpha$ ) and  $I$ -dependent kinetic order ( $\beta$ ) can also be determined by piecewise  $\ln k_{\text{LH}}\text{--}\ln I$  fitting [29,30,69] as per Eq. (13).

$$K_{\text{ads}}^{\text{app}} = 1/K_{\text{diss}}^{\text{app}} = \frac{k_1}{k_{-1} + \alpha I^\beta} \Rightarrow \frac{1}{K_{\text{ads}}^{\text{app}}} = \frac{k_{-1}}{k_1} + \frac{\alpha I^\beta}{k_1} \Rightarrow \frac{1}{K_{\text{ads}}^{\text{app}}}$$

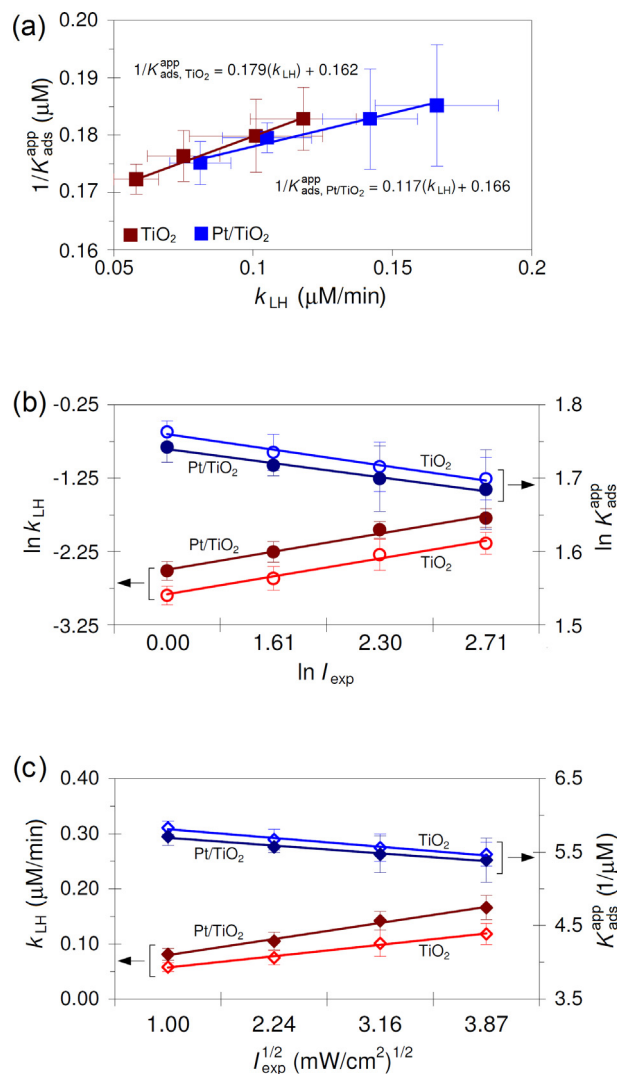


**Fig. 6.** (a) Plots of  $1/K_{\text{ads}}^{\text{app}}$  and  $1/k_{\text{LH}}$  for bare and Pt-photodoped  $\text{TiO}_2$ , the optimized fit values for  $k_1$ ,  $k_{-1}$ , and  $K_{\text{ads}}^{\text{app}}$  (Eq. (12)) are summarized in Table 3; (b) plots of  $\ln k_{\text{LH}}$  and  $\ln K_{\text{ads}}^{\text{app}}$  as a function of  $\ln I_{\text{exp}}$ , the values of  $\alpha$  and  $\beta$  from piece-wise fitting (Eq. (13)) are summarized in Table 3; and (c) dependence of  $k_{\text{LH}}$  and  $K_{\text{ads}}^{\text{app}}$  on the square root of irradiance. (For interpretation of the references to colour in this figure legend, the reader is referred to the web version of this article.).

$$= \frac{1}{k_1} \cdot k_{\text{LH}} + \frac{k_{-1}}{k_1} \quad (12)$$

$$k_{\text{LH}} = \alpha \cdot I^\beta \Rightarrow \ln k_{\text{LH}} = \beta \cdot \ln I + \ln \alpha = \beta \cdot \ln I + \ln \left( \frac{k_{\text{LH}} K_{\text{ads}}^{\text{app}} C_0}{1 + K_{\text{ads}}^{\text{app}} C_0} \right) \quad (13)$$

whereas Eqs. (11) (12) were originally used to estimate kinetic parameter values for liquid-phase reactions where oxidative transformations are mediated mainly by  $\text{OH}^\bullet$  [24], present use for gas-phase photoreaction where  $\text{O}_2^\bullet$  predominates also yielded consequential findings. By plotting suitably transformed classic L–H kinetic parameter values for  $\text{TiO}_2$  and  $\text{Pt/TiO}_2$  (Table 2, Fig. 6a), determination of optimized fit parameter values was straightforward. The  $\ln$ -transform plots (Fig. 6b), while allowing for the estimation of  $\alpha$ - and  $\beta$ -values, also yielded spatially distinct curve fits than the irradiance-square plots (Fig. 6c) when values for  $\text{TiO}_2$  and  $\text{Pt/TiO}_2$  were plotted simultaneously.

As shown in Table 3, estimated  $K_{\text{ads}}$  values suggest better  $\text{CS}_2$  affinity with bare  $\text{TiO}_2$  ( $6.18/\mu\text{M}$ ) than  $\text{Pt/TiO}_2$  ( $6.01/\mu\text{M}$ ) even



**Table 3**

CS<sub>2</sub> photodegradation optimized fit parameter values based on the pseudo-steady-state model with untreated and 0.5 wt% photodoped TiO<sub>2</sub> at different UV intensities.<sup>a</sup>

	TiO <sub>2</sub>	Pt/TiO <sub>2</sub>
$k_{-1}/k_1$ (μM) <sup>b</sup>	0.162	0.166
$k_1$ (1/min) <sup>b</sup>	5.57	5.65
$k_{-1}$ (μM/min) <sup>b</sup>	0.901	0.940
$K_{ads}$ (1/μM) <sup>b</sup>	6.18	6.01
$\alpha^c$ (M/min) at $I_{exp}$ =		
0–1	$6.67 \times 10^{-9}$	$7.72 \times 10^{-9}$
1–5	$4.80 \times 10^{-8}$	$6.25 \times 10^{-8}$
1–10	$4.57 \times 10^{-8}$	$6.07 \times 10^{-8}$
5–15	$6.12 \times 10^{-8}$	$8.56 \times 10^{-8}$
$\beta^c$ (unitless) at $I_{exp}$ =		
0–1	0.87	1.09
1–5	0.22	0.26
1–10	0.26	0.28
5–15	0.23	0.25

<sup>a</sup> [CS<sub>2</sub>]<sub>0</sub> = 8.3–165.5 μM, uncollimated UV ( $d_{exp}$  = 2 cm), and  $t$  = 25 min.

<sup>b</sup> Derived from  $1/K_{ads}^{app} - 1/k_{LH}$  plots in Fig. 6a and Eq. (12).

<sup>c</sup> Derived from  $\ln k_{LH} - \ln I_{exp}$  plots in Fig. 6b and Eq. (13).

in the absence of irradiation presumably due to reduced access to active sites as a result of Pt deposition, in agreement with  $K_{ads}^{app}$  trends (Table 2) for both catalysts at irradiated conditions. Higher  $k_1$  and  $k_{-1}$  values with Pt/TiO<sub>2</sub> (5.57/min, 0.901 μM/min)

than TiO<sub>2</sub> (5.65/min, 0.940 μM/min) would have been afforded by the unique but complementary roles of desired OH groups and surface deposited Pt in effecting better conversion rates. Estimated  $\alpha$ - and  $\beta$ -values from nonlinear data fitting show distinct transition between the 0–1 and 1–5 mW/cm<sup>2</sup> range wherein the tenfold increase of  $I$ -independent reaction rate ( $\alpha$ -value of  $10^{-9}$ – $10^{-8}$  M/min) coincided with the plateauing of  $I$ -dependent kinetic order ( $\beta$ -value of  $\sim 1$ – $\sim 0.25$ ) for both TiO<sub>2</sub> and Pt/TiO<sub>2</sub>. Although slight differences of  $\alpha$ - and  $\beta$ -values between catalysts can well be a function of surface and photon absorption characteristics, observed transitions are attributed to the predominance of de-excitation at  $I > 1$  mW/cm<sup>2</sup> wherein reaction orders are typically sub-unity, in agreement with previous findings [30,69]. This corroborates well with the impact of irradiance level as predicted by the simplified RFM in tandem with amended L–H kinetics, highlighting the fact that use of strong illumination is neither advantageous nor economically practical [24]. It was also shown that  $k_{LH}$  range (Table 2) is of similar order as  $k_{-1}$  (Table 3), even tenfold at  $I < 10$  mW/cm<sup>2</sup>, suggesting that the pseudo-steady-state analysis was vindicated since classic equilibrium calculations have underestimated apparent maximum rates ( $k_{LH}$ ). On the other hand, increased conversion and photonic efficiencies (Table 4) was more or less related to calculated  $k_{LH}$  values irradiance-wise with elevated values obtained for Pt/TiO<sub>2</sub> whereas plausible mechanisms were proposed earlier (Section 3.4).

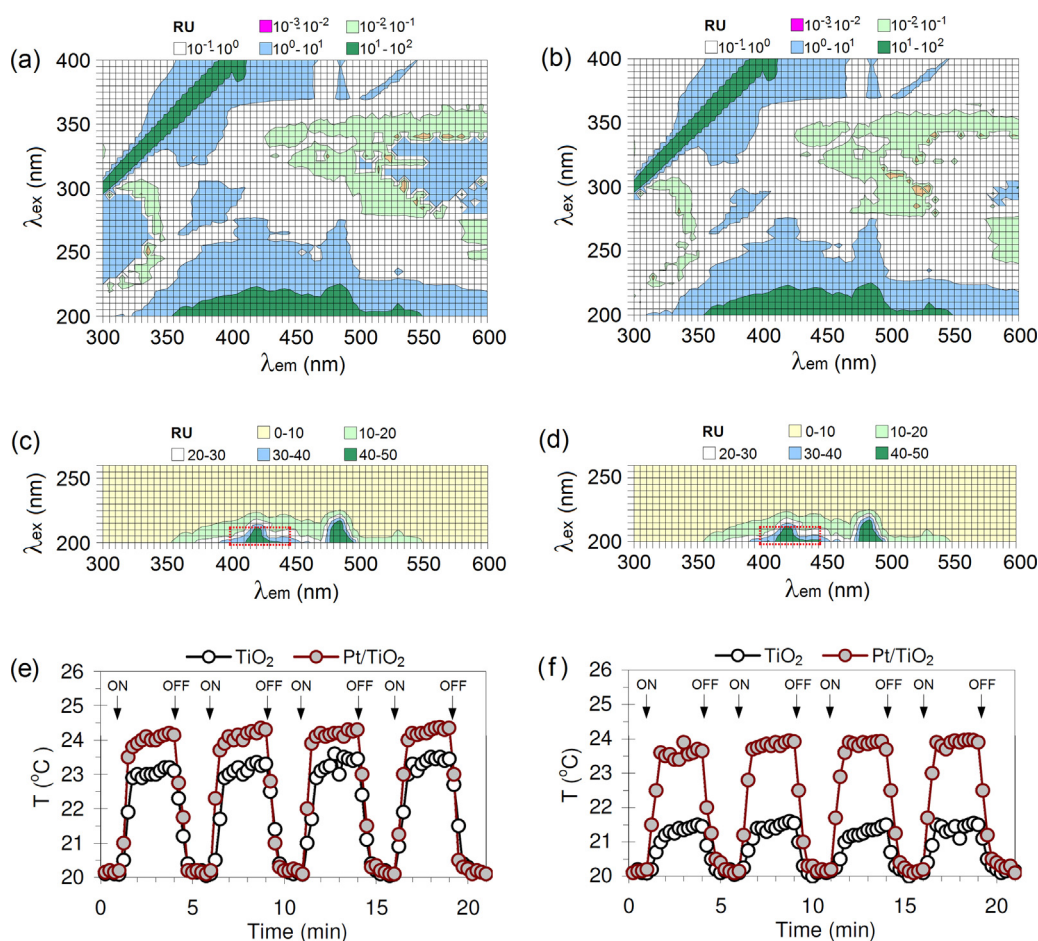


**Fig. 7.** Upper panel: Fluorescence EEM profile of (a) untreated and (b) 0.5 wt% photodoped TiO<sub>2</sub> with fluorescence responses in log<sub>10</sub> Raman units (RU). Middle panel: portion of the fluorescence EEM profile of (c) untreated and (d) 0.5 wt% photodoped TiO<sub>2</sub> with fluorescence responses in RU (highlighted). Lower panel: timewise temperature profile of the same photocatalysts illuminated with (e) 365-nm UV light at  $I_{exp} = 40$  mW/cm<sup>2</sup> and (f) 455-nm visible light at  $I_{exp} = 0.9$  W/cm<sup>2</sup> at intervals of 3-min on and 2-min off. (For interpretation of the references to colour in this figure legend, the reader is referred to the web version of this article.)

**Table 4**

CS<sub>2</sub> conversion efficiencies (% conversion) and photonic efficiencies (%  $\zeta$ ) with untreated and 0.5 wt% photodoped TiO<sub>2</sub> at different UV intensities.<sup>a</sup>

	TiO <sub>2</sub>	Pt/TiO <sub>2</sub>
%conversion <sup>b</sup> at $I_{\text{exp}}$ =		
1	5.9–27.8	9.2–39.1
5	8.7–37.7	13.4–52.9
10	11.7–45.9	18.1–64.3
15	18.1–53.4	27.7–74.8
% $\zeta$ <sup>c,d</sup> (moles/einstein) at $I_{\text{exp}}$ =		
1	0.0047–0.020	0.0066–0.0309
5	0.0064–0.0293	0.0089–0.0452
10	0.0078–0.0396	0.0109–0.0608
15	0.0091–0.0606	0.0126–0.0933

<sup>a</sup> Uncollimated UV ( $d_{\text{exp}} = 2$  cm) and  $t = 25$  min.

<sup>b</sup> Values correspond to decreasing initial CS<sub>2</sub> concentration, [CS<sub>2</sub>]<sub>0</sub> = 165.5–8.3  $\mu$ M.

<sup>c</sup> Values correspond to increasing initial CS<sub>2</sub> concentration, [CS<sub>2</sub>]<sub>0</sub> = 8.3–165.5  $\mu$ M.

<sup>d</sup> See Eq. (10).

### 3.6. Plasmon-driven photocatalysis

It is widely known that photoreactivity is enhanced by dispersing noble metal nanoparticles into semiconductor photocatalysts, resulting in the occurrence of a Schottky junction and LSPR. The Schottky junction suppresses de-excitation whereas LSPR effects such as  $e$ – $h$  excitation and localized heating, among other effects, enhance photocatalysis; ref. [70] details on underlying mechanisms. Unlike Ag and Au, of known LSPR characteristics in the vis-NIR region, the LSPR mode of Pt is in the UV range. In order to demonstrate the occurrence of LSPR effects in Pt/TiO<sub>2</sub>, fluorescence EEM matrices and local heating profiles were obtained. Logarithmic plot for TiO<sub>2</sub> in Fig. 7a show distinct fluorescence clusters at  $\lambda_{\text{ex}} = 225$ –300/ $\lambda_{\text{em}} = 300$ –340 and  $\lambda_{\text{ex}} = 300$ –340/ $\lambda_{\text{em}} = 525$ –600 which are not present in Pt/TiO<sub>2</sub>. The size range of titania nanoparticulate sizes also resulted in conspicuous Rayleigh-Tyndall streak ( $\lambda_{\text{ex}}, \lambda_{\text{em}} = 300$ –400). The two distinct ranges of  $\lambda_{\text{ex}}$  (RU  $\approx 10^0$ – $10^1$ ) coincide with the two regimes of maximal absorbance for TiO<sub>2</sub> in Fig. 2d of which values exceed those of Pt/TiO<sub>2</sub>, marked by the disappearance of said fluorescence clusters in Pt/TiO<sub>2</sub>. Interestingly, an overall reduction of fluorescence values within the order of  $10^0$ – $10^1$  RU correlates well with the Raman peak intensities (TiO<sub>2</sub> > Pt/TiO<sub>2</sub>) in Fig. 2b, attributed to the electron trapping role of surface adsorbed Pt (better  $e$ – $h$  separation). However, these logarithmic plots (Fig. 7a and b) are not able to show distinct differences in fluorescence values in the range of  $10^1$ – $10^2$  RU. The decimal plots (Fig. 7c and d) rather show slight increase of fluorescence ( $\lambda_{\text{ex}} = 200$ –210/ $\lambda_{\text{em}} = 400$ –445), perhaps tantamount to the low amount of Pt dopant but nevertheless suggestive of enhanced  $e$ – $h$  generation due to the UV plasmonic behavior of Pt. The prominent emissions at around 421 nm and 491 nm was attributed to the recombination of  $e$ – $h$  due to dangling bonds in TiO<sub>2</sub> while the emission at around 534 nm was attributed to oxygen vacancies [71]. On the other hand, IR thermography profiles (Fig. 7e and f) show better LSPR-mediated localized heating at a resonance wavelength in the UV (365 nm) rather than the visible (455 nm) region. At 365 nm and power output of 40 mW/cm<sup>2</sup>, the UV induced localized heating in Pt/TiO<sub>2</sub> ( $\sim 24^\circ\text{C}$ ) was higher than that of TiO<sub>2</sub> ( $\sim 23^\circ\text{C}$ ) by  $\sim 1^\circ\text{C}$  (Fig 7e). Only the use of 20-fold output power (0.9 W/cm<sup>2</sup>) did result in comparable heating in Pt/TiO<sub>2</sub>, with substantial temperature gap observed between TiO<sub>2</sub> ( $\sim 21^\circ\text{C}$ ) and Pt/TiO<sub>2</sub> ( $\sim 23.5^\circ\text{C}$ ), during irradiation at 455 nm (Fig 7f). Despite the low levels of photodoped Pt, the use of fluorescence EEM analysis and IR thermography somehow supported a scenario of photocatalysis driven by LSPR effects. Use of the coupled techniques can be extended in the study of plasmonic behaviors of a range of noble metal dopants in conjunction with studies on photoreaction kinetics.

## 4. Conclusions

This work has reported for the first time a radiation field model of optical fiber-coupled LED–UV, either uncollimated or collimated, with respect to photocatalyst covered surface and the subsequent use in the photodegradation of CS<sub>2</sub> as model odorant with titania based photocatalyst. Use of a simple method of surface deposition via UV photoreduction, the photocatalytic capacity of widely available anatase TiO<sub>2</sub> was enhanced by the surface deposited Pt. Results of fixed irradiance experiments with bare anatase TiO<sub>2</sub>, namely the enhanced gas-phase CS<sub>2</sub> photooxidation rates with collimated optically channeled LED–UV radiation, were sufficiently accounted for by radiation field model predictions. Higher resultant irradiance, effecting enhanced reaction rates, was attributed to reduced divergence and focusing of the collimated UV output beam. Magnification of irradiance was dependent on geometrical optics as a function of optical fiber and collimator specifications regardless of source photopower. Use of optic fiber-coupled LED–UV nevertheless affords flexibility with regards to photoradiation source positioning in photoreactor design while collimation magnifies the photopower from photoradiation source apparent, further extending photonic efficiency in photocatalytic applications beyond the present photooxidative deodorization. Thus obtained parameter values from the classic L–H kinetics suggest slightly decreased CS<sub>2</sub> affinity to Pt/TiO<sub>2</sub> ( $K_{\text{ads}}^{\text{app}} \sim 98\%$  that of TiO<sub>2</sub>), understood due to portion of active sites in Pt/TiO<sub>2</sub> being blocked by surface deposited Pt. The setback in adsorptive affinity was outweighed by the dramatic increase of reaction rate with Pt/TiO<sub>2</sub> ( $k_{\text{LH}} \sim 140\%$  that of TiO<sub>2</sub>) presumably due to LSPR related effects imparted by surface deposited Pt. Best fit parameter values from the amended L–H type kinetics using the pseudo-steady-state model yielded similar trends in  $K_{\text{ads}}-k_{\text{LH}}$  values, nonetheless showing these were underestimated in classic L–H kinetic modeling. The amended model also showed that modulated LED–UV irradiance resulted in non-linearly proportional reaction rates and photonic efficiencies in CS<sub>2</sub> photooxidation. Calculated reaction orders approached unity at  $I_{\text{exp}} \leq 1$  mW/cm<sup>2</sup> and were about 0.25 at  $I_{\text{exp}} > 1$  mW/cm<sup>2</sup>. Hallmarks of LSPR occurrence were for the first time innovatively probed by fluorescence EEM spectroscopy in tandem with IR thermography. Accordingly, Pt-stimulated LSPR effects as manifested by localized heating and suppressed  $e$ – $h$  recombination has enhanced the photocatalytic power of anatase titania.

## Acknowledgments

The authors acknowledge financial support through the UNSW Vice-Chancellors Research Fellowship (RG124341) and the UNSW Faculty of Engineering Early Career Research grant (PS35136). The authors also acknowledge the technical support from the UNSW Mark Wainwright Analytical Centre in solid state and elemental analyses. AJ Anceno would like to thank the UNSW Water Research Centre's X Wang, G Parcsi, E Sivret, H Le, N Le-Minh, D Roser, G Lui, M Bligh, and T Liu; the UNSW Structural Engineering's MM Gharib; and the UNSW Photonics and Optical Communications' Y Luo for the discussions and technical advice.

## References

- [1] K. Harada, A. Hasegawa, C.N. Wei, et al., J. Health Sci. 56 (2010) 488.
- [2] A. Luengas, A. Barona, C. Hort, et al., Rev. Environ. Sci. Biotechnol. (2015), in press.
- [3] P. Wolkoff, C.K. Wilkins, P.A. Clausen, et al., Indoor Air 16 (2006) 7.
- [4] M. Cambra-López, A.J.A. Aarnink, Y. Zhao, et al., Environ. Pollut. 158 (2010) 1.
- [5] E.Z. Harrison, Biocycle 48 (2007) 44.
- [6] R. Lebrero, L. Bouchy, R. Stuetz, et al., Crit. Rev. Environ. Sci. Technol. 41 (2011) 915.
- [7] A. Noyola, J.M. Morgan-Sagastume, J.E. López-Hernández, Rev. Environ. Sci. Biotechnol. 5 (2006) 93.

- [8] G.R. Parmar, N.N. Rao, *Crit. Rev. Environ. Sci. Technol.* 39 (2009) 41.
- [9] W.Y. Teoh, J.A. Scott, R. Amal, *J. Phys. Chem. Lett.* 3 (2012) 629.
- [10] A.O. Ibhadon, P. Fitzpatrick, *Catalysts* 3 (2013) 189.
- [11] J. Mo, Y. Zhang, Q. Xu, et al., *Atmos. Environ.* 43 (2009) 2229.
- [12] O. Tokode, R. Prabhu, L.A. Lawton, et al., *Appl. Catal. B: Environ.* 156–157 (2014) 398.
- [13] O.I. Tokode, R. Prabhu, L.A. Lawton, et al., *J. Catal.* 290 (2012) 138.
- [14] W.K. Jo, R.J. Tayade, *Ind. Eng. Chem. Res.* 53 (2014) 2073.
- [15] J.R. Lombardi, R.L. Birke, *J. Phys. Chem. C* 112 (2008) 5605.
- [16] Z. Wang, J. Liu, W. Chen, *Dalton T.* 41 (2012) 4866.
- [17] V.P. Zhdanov, C. Häggglund, B. Kasemo, *Surf. Sci.* 599 (2005) L372.
- [18] C. Langhammer, Z. Yuan, I. Zorić, et al., *Nano Lett.* 6 (2006) 833.
- [19] S. Sun, W. Wang, L. Zhang, et al., *Catal. Commun.* 11 (2009) 290.
- [20] P. Christopher, H. Xin, S. Linic, *Nat. Chem.* 3 (2011) 467.
- [21] D.F. Ollis, *J. Phys. Chem. B* 109 (2005) 2439.
- [22] A. Mills, J. Wang, D.F. Ollis, *J. Phys. Chem. B* 110 (2006) 14386.
- [23] A. Mills, J. Wang, D.F. Ollis, *J. Catal.* 243 (2006) 1.
- [24] D. Ollis, *Photocatalytic treatment of water: irradiance influences*, in: P. Pichat (Ed.), *Photocatalysis and Water Purification*, Wiley-VCH, Weinheim, Germany, 2013, p. 313.
- [25] A. Hambly, *Fluorescence as a Portable Tool for Cross-connection Detection within Dual Reticulation Systems*, School of Civil and Environmental Engineering, The University of New South Wales, Sydney, Australia, 2013.
- [26] G. Li Puma, J.N. Khor, A. Brucato, *Environ. Sci. Technol.* 38 (2004) 3737.
- [27] M.A. Mueses, F. Machuca-Martinez, A. Hernández-Ramírez, et al., *Chem. Eng. J.* 279 (2015) 442.
- [28] M.A. Mueses, F. Machuca-Martinez, G. Li Puma, *Chem. Eng. J.* 215–216 (2013) 937.
- [29] I. Salvadó-Estivill, D.M. Hargreaves, G. Li Puma, *Environ. Sci. Technol.* 41 (2007) 2028.
- [30] Z. Wang, J. Liu, Y. Dai, et al., *Ind. Eng. Chem. Res.* 50 (2011) 7977.
- [31] Z. Wang, J. Liu, Y. Dai, et al., *J. Hazard. Mater.* 25 (2012) 215–216.
- [32] O. Muzychko, *Proc. SPIE* 6672 (2007) art. no. 66,720X.
- [33] L. Svilainis, *Measurement* 41 (2008) 647.
- [34] G.W. Chang, C.C. Liao, Y.C. Chen, *Proc. SPIE* 7717 (2010), art. no. 77,171F.
- [35] D.F. Ollis, E. Pelizzetti, N. Serpone, *Environ. Sci. Technol.* 25 (1991) 1523.
- [36] N. Serpone, *J. Photochem. Photobiol. A Chem.* 104 (1997) 1.
- [37] G. Sagawe, M.L. Satuf, R.J. Brandi, et al., *Ind. Eng. Chem. Res.* 49 (2010) 6898.
- [38] A. Alonso-Tellez, D. Robert, N. Keller, et al., *Appl. Catal. B Environ.* 115–116 (2012) 209.
- [39] K. Demeestere, J. Dewulf, B. De Witte, et al., *Appl. Catal. B Environ.* 60 (2005) 93.
- [40] C.H. Yu, C.S. Chen, H.C. Shei, *Sust. Environ. Res.* 20 (2010) 375.
- [41] B. Ohtani, O.O. Prieto-Mahaney, D. Li, et al., *J. Photochem. Photobiol. A Chem.* 216 (2010) 179.
- [42] T.O. Peyton, R.V. Steele, W.R. Mabey, *Carbon Disulfide*, in: *Carbonyl Sulfide: Literature Review and Environmental Assessment*, EPA - OHEE, Washington, D.C, 1978.
- [43] WHO, *Air Quality Guidelines for Europe*, second ed., W.H.O. Regional Publication, Copenhagen, 2000 (European Series no. 91).
- [44] H.P. Gelbke, T. Göen, M. Mäurer, et al., *Crit. Rev. Toxicol.* 39 (2009) 1.
- [45] M. De Sogno, A.J. Yarwood, O.P. Strausz, et al., *Can. J. Chem.* 43 (1965) 1886.
- [46] W.P. Wood, J. Heicklen, *J. Photochem.* 2 (1973) 173.
- [47] W.P. Wood, J. Heicklen, *J. Phys. Chem.-U S* 75 (1971) 854.
- [48] J.J. Colman, W.C. Troglor, *J. Am. Chem. Soc.* 117 (1995) 11270.
- [49] J.J. Colman, W.C. Troglor, *J. Geophys. Res. -Atmos.* 102 (1997) 19029.
- [50] J.A. Logan, M.B. McElroy, S.C. Wofsy, et al., *Nature (Lond.)* 281 (1979) 185.
- [51] K.H. Becker, W. Nelsen, Y. Su, et al., *Chem. Phys. Lett.* 168 (1990) 559.
- [52] T.P. Murrells, E.R. Lovejoy, A.R. Ravishankara, *J. Phys. Chem.-US* 94 (1990) 2381.
- [53] E.R. Lovejoy, T.P. Murrells, A.R. Ravishankara, et al., *J. Phys. Chem.-US* 94 (1990) 2386.
- [54] R.E. Stickel, M. Chin, E.P. Daykin, et al., *J. Phys. Chem.-US* 97 (1993) 13653.
- [55] Y. Bai, W. Li, C. Liu, et al., *J. Mater. Chem.* 19 (2009) 7055.
- [56] R.A. Naphade, M. Tathavadekar, J.P. Jog, et al., *J. Mater. Chem. A* 2 (2014) 975.
- [57] I. Becker, I. Hofmann, F.A. Müller, *J. Eur. Ceram. Soc.* 27 (2007) 4547.
- [58] K.V. Baiju, S. Shukla, S. Biju, et al., *Catal. Lett.* 131 (2009) 663.
- [59] J. Shi, J. Chen, Z. Feng, et al., *J. Phys. Chem. C* 111 (2007) 693.
- [60] E. McCafferty, J.P. Wightman, *Surf. Interface Anal.* 26 (1998) 549.
- [61] C.G. Silva, J.L. Faria, *Photochem. Photobiol. Sci.* 8 (2009) 705.
- [62] F.B. Li, X.Z. Li, *Chemosphere* 48 (2002) 1103.
- [63] Y. Jiang, J. Scott, R. Amal, *Appl. Catal. B Environ.* 126 (2012) 290.
- [64] Y. Jiang, R. Amal, *Appl. Catal. B Environ.* 138–139 (2013) 260.
- [65] M. Takeuchi, T. Kimura, M. Hidaka, et al., *J. Catal.* 246 (2007) 235.
- [66] H. Zhang, H. Yu, A. Zheng, et al., *Environ. Sci. Technol.* 42 (2008) 5316.
- [67] Q. Wang, M. Zhang, C. Chen, et al., *Angew. Chem. Int. Ed.* 49 (2010) 7976.
- [68] H. Wang, Q. Zhang, I.G. Dalla Lana, et al., *J. Chromatogr. Sci.* 36 (1998) 605.
- [69] G. Vincent, P.M. Marquaire, O. Zahraa, *J. Photochem. Photobiol. A Chem.* 197 (2008) 177.
- [70] X. Zhang, Y.L. Chen, R.S. Liu, et al., *Rep. Prog. Phys.* 76 (2013).
- [71] S. Mathew, A. Kumar Prasad, T. Benoy, et al., *J. Fluoresc.* 22 (2012) 1563.